Accepted Manuscript

Title: Smectite clay microtructural behaviour on the Atterberg limits transition

Author: Marek S. Żbik David J. Williams Yen-Fang Song Chun-Chieh Wang

Please cite this article as: M.S. Żbik, D.J. Williams, Y.-F. Song, C.-C. Wang, Smectite clay microtructural behaviour on the Atterberg limits transition, *Colloids and Surfaces A: Physicochemical and Engineering Aspects* (2014), http://dx.doi.org/10.1016/j.colsurfa.2014.11.042

Smectite clay microtructural behaviour on the Atterberg limits transition

Marek S. Żbik[a,*], David J. Williams[a], Yen-Fang Song[b], Chun-Chieh Wang[b]

[a]*Geotechnical Engineering Centre, The University of Queensland, St Lucia, Brisbane 4072, Australia*

[b]*National Synchrotron Radiation Research Center, 101 Hsin-Ann Road, Hsinchu Science Park, Hsinchu 30076, Taiwan, R.O.C.*

*Corresponding author. E-mail: m.zbik@uq.edu.au, song@nsrrc.org.tw

Abstract: Particle space arrangement is a very important factor that determines the physico-mechanical properties of soil. Formations of three-dimensional (3D) structured networks within gelled or flocculated suspension may prevent clay particles and aggregates from building dense aggregates and by encapsulate water within the ultrathin and closed void network, lead to poor sludge dewatering. To better understand the water retention behaviour of smectite-rich clays, a microstructural investigation was conducted on Amcol Australian bentonite in aqueous suspension in near the liquid limit (LL) and the plastic limit (PL). The investigation was conducted with the aid of synchrotron-powered transmission x-ray microscope tomography (TXM), with subsequent computer reconstruction. Images from the microscopy studies were statistically analysed using the STatistical IMage ANalysing (STIMAN) system. The study found that clay particles form a spanned framework in which mineral particles, aggregates and water-filled voids assemble as hierarchic structural elements. The size of these structural elements was larger in the water suspension and subsequently became smaller as an effect of water loss in the suspension > liquid and > plastic limit conditions. The clay suspension structure was almost isometric, with a low anisotropy coefficient: Kα - 9%. This parameter increased to Kα - 17% in (LL) and increased further in (PL) conditions to Kα - 35%. Voids within structural elements were much smaller than the water filled inter-flock voids, with their median diameter 140 nm (suspension), 120 nm (LL) and 90 nm (PL). Significant differences in Atterberg limits values were observed between powder freshly mixed with water and a seasoned sample. Therefore, careful consideration of the sample mineral composition, clay content and genesis must be given due to preparation for geotechnical examination.

1. Introduction

The term 'soil' is universally used across many disciplines of science. In general, it refers to the uncompacted layer of bedrock fragment covering the surface of the crust of planetary bodies and known by the name of a 'regolith'. Since Wesselink [1] estimated the grain size of the lunar regolith in 1948, studies of planetary regoliths have been conducted not only on Earth but also on the moon and Mars.

The term 'soil' is most commonly used in agriculture, where it can be synonymous with rich organic topsoil for plant growing, and in engineering geology (civil engineering), where soil is synonymous with the ground on or in which a range of engineering structures are built. In this sense, soil is used to support structures and embankments, as a construction material, and for other anthropogenic activities [2].

Clay-rich soils that contain more than 2 wt% of clay minerals need to be treated carefully when it comes to these activities. Clay-rich soils have different characteristics from many other regoliths and, as a result, behave differently. These characteristics often have a damaging effect on engineering structures. Generally, these soils behave as semisolids within a certain range of water content, and their physical properties change gradually as the moisture content changes. When water is added, clay-rich soils can gradually transform from a semisolid state through a plastic state to a semiliquid state. Each of these states can be determined by defined parameters, such as shrinkage limit (SL), plastic limit (PL) and liquid limit (LL). The detailed definitions of these parameters are called the Atterberg limits [3].

The Swedish scientist A. Atterberg established several specific methods for classifying and describing the behaviour of cohesive soils like clays under various moisture condition. The laboratory procedures used by Atterberg shortly after the turn of the twenty century, to determine the liquid limit and plastic limit of soil tests are in use today by soil engineers around the world.

The liquid limit and plastic limit tests define the upper and lower moisture content points at which a particular soil ceases to perform as a plastic [4, 5].

The LL is determined by measuring the water content and the numbers of blows required to close a specific grove for a certain length in a standard LL Casagrande device. The PL is determined my measuring the water content of the soil when threads of the soil 3 mm in diameter begin to crumble. These two limits are vital soil characteristic because they determine how much water may be retained in the soil before liquification. The difference in the water content between these two limits is called the plasticity index (PI); it contains information about how much water can be retained in a soil before it transforms from a semisolid state to a semiliquid state. This is important because this transformation can have catastrophic consequences for engineering structures supported by the soil.

Little is known about the mechanisms behind these transformations because the clay particles are in general too small for optical observation and in the wet stage, soil samples are not suitable for investigation using most electron microscope techniques. To better understand the behaviour of clay-rich soil in the transition between semisolid and semiliquid stages, the high smectite content clay soil was investigated using a transmission x-ray microscope (TXM). Investigations were conducted in different water-capacity stages that mimicked the LLs and PLs used in engineering practice.

Structural transformations between all these stages were the subject of observation at the micro scale using synchrotron-powered TXM with subsequent computer three-dimensional (3D)

2

reconstruction. The results of these observations from 3D space images and image sections as well as statistical image analyses were the focus of the present study.

2. Experimental section

Commercially available Australian 'Amcol' sodium smectite, clay-rich bentonite, was chosen for this study. The product was sourced from Amcol Australia Pty Ltd, which owns and operates an Upper Jurassic bentonite mine at Miles in Queensland, approximately 375 kilometres north-west of Brisbane [6]. From non-treated bentonite, a 2.5 wt% suspension was prepared in deionised water (DI) and was sonicated for one-minute with 50 W power. The pH was not controlled and measured approximately 8 in suspension.

Sample preparation for plastic and liquid limit condition was conducted by adding water to dry soil and working it by spatula accordingly to procedures described in [3, 4, 5,].The electrokinetic potential (zeta potential or ζ) was measured in the clay samples using a Zetasizer (NanoSeries), manufactured by Malvern Ltd, United Kingdom. Samples of diluted suspension (~0.2 wt%) were prepared from the clay fraction and inserted into the disposable measurement cell. The zeta potential in mV and electric conductivity in mS/cm were measured in DI water. For comparison results of the zeta potential was also measured in 0.1 M NaCl and $CaCl_2$ salt suspensions. Measurements were made following the procedures as described in Hunter [7], Lyklema [8] and Minor et al. [9].

X-ray diffraction (XRD) patterns were recorded with a PANalytical X'Pert Pro, a multi-purpose diffractometer using Fe filtered Ca Ka radiation, an auto divergence slit, a 2° anti-scatter slit and a fast X'Celerator Si strip detector. The diffraction patterns were recorded in steps of 0.016° 2-theta with a 0.4 second counting time per step, and logged to data files for analysis.

Electron microscope investigations were conducted using a JEOL-2100 transmission electron microscope (TEM) operating with a 200 kV accelerating potential. A scanning electron microscope (SEM) JEOL 6040 was used to investigate samples coated in platinum film with accelerating voltage 15–20 kV. For 3D imaging, a Cryo-TEM was used with an accelerating voltage of 300 kV. The aqueous suspension samples were vitrified at liquid nitrogen temperature by rapidly plunging the samples into an environment-stable camera (stable temperature and moisture content).

TXM proved to be an efficient instrument for studying the internal structure of nano-material because of its large penetration depth and superior spatial resolution. TXM, which was used in the present study, has been installed on the synchrotron at Taiwan's National Synchrotron Radiation Research Center [10, 11]. This TXM provides two-dimensional (2D) imaging and 3D tomography at an energy of 8–11 keV, with a spatial resolution of 50–60 nm and with the Zernike-phase contrast capability to image light material that lacks X-ray absorption contrast. TXM allows the measurements of aqueous specimens because it has no vacuum requirement.

The photon energy of 8 keV was used to image the clay suspension for maximum X-ray absorption. The exposure time of a 2D image is 15 seconds to 4 minutes. By acquiring a series of

3

2D images with the sample rotated stepwise, 3D tomography datasets were reconstructed based on 141 sequential image frames taken in first-order diffraction mode with the azimuth angle rotating from −70º to +70º for the lateral plate specimen.

Images from the microscopy studies were statistically analysed using the STatistical IMage ANalysing (STIMAN) system [12–15] technique, which has been adapted for studying clay suspensions. This technique can extract integrated information on sample microstructures, especially on total pore (void) space and the spread of micropore sizes. It contains a subroutine for estimating filtration properties from the void space parameters. Examples of the output parameters include: examined void number; porosity (%); total void/particle area (sq. µm); total void perimeter (µm); average diameter (µm); average perimeter (µm) the form index (K_f) (platelet thickness to diameter); and the structure element orientation (K_α) [16].

In the present study, the use of the STIMAN technique was limited to obtaining statistical information about porosity, particle average diameter and pore distribution according to their total area from 2D micrographs. The 3D STIMAN technique was also used to estimate flock size in suspension.

TXM images such as those shown in Fig. 2 carry information about a suspension layer approximately 50 µm in thickness. All samples are uniform in composition; therefore, the only differences seen in consequent images photographed from different angles is information about flock packing density. As density differs from water to particles or flocked aggregates, information about space particle packing can be transposed from 3D space images to diagrams of structural element dimensions, as shown in the results.

3. Results and discussion

3.1. General characterisation

The results of the electron microscope morphology studies and elemental composition are shown in Fig. 1. The TEM micrograph (Fig. 1A) shows a small aggregate of smectite flakes approximately 2 µm in diameter. These flakes are very thin and flexible, displaying numerous wrinkles and ragged, highly transparent edges. Extremely dispersed plate-like particles, of diameters from a few nm to 200 nm, form a continuous film on which is placed the larger aggregate of sheet ca 2 µm in diameter, seen in the centre of the micrograph. Highly dispersed particles may be the result of smectite flake erosion, halloysite tubes are also present. In the SEM micrograph (Fig. 1B), smectite flakes of diameters below one µm are clearly part of the small and compact primary bentonite rock fragments. The XRD results displayed in Fig. 1C exhibit smectite (78%), with a small presence of quartz (10%), anorthite (8%), kaolinite (4%) and anatase. Major indexation shown in Fig 1C.

Zeta potential and electric conductivity measurements conducted in DI water, 0.1 M NaCl and $CaCl_2$ on 'Amcol' smectite demonstrate a gradual reduction of a negative zeta potential with a simultaneous increase of the solution's ionic strength.

4

Table 1. Electrokinetic potential and electric conductivity of studied smectite sample in natural pH~8

|	Zeta potential in mV	Electric conductivity in mS/cm
DI water	−61,4	0,00144
0,1M NaCl	−39,6	13
0,1 M CaCl$_2$	−12,6	22,6
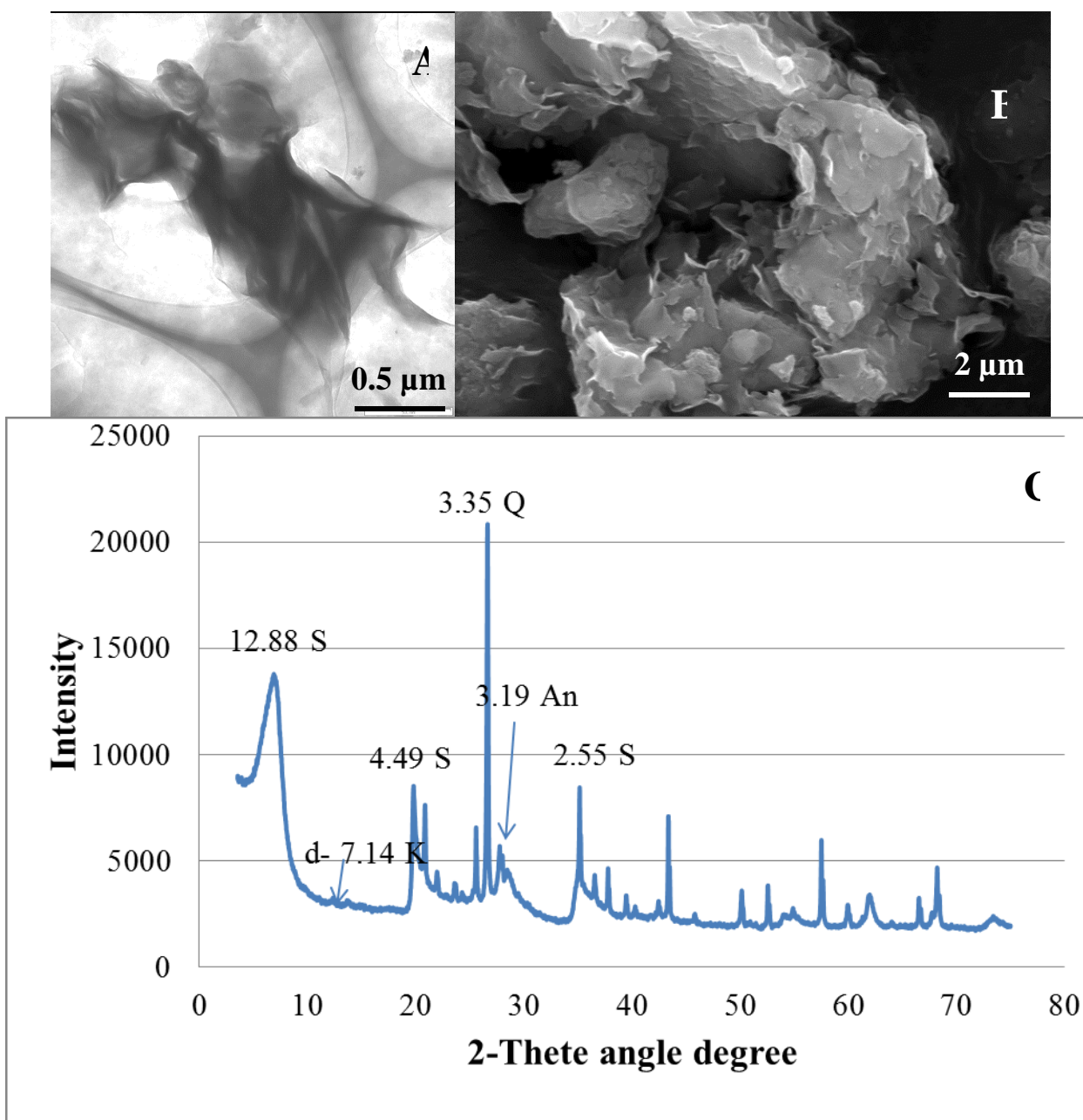
Fig. 1. (A) The TEM micrograph shows a small aggregate of 'Amcol' smectite flakes ca. 2 μm in diameter and much smaller plate-like particles seen on a background of particles below 100 nm; (B) SEM micrographs show a smectite primary aggregate that displays flexible smectite flakes just below 1 μm in diameter; (C) The XRD diffractogram shows the presence of smectite (S) as the major constituent alongside a small admixture of quartz (Q), anorthite (An), kaolinite (K) and anatase.

Density measurements conducted with a helium pycnometer demonstrate an average value of 2.355 g/cm^3. The Atterberg limits conducted on the sample without aging demonstrate (PL) 20%, (LL) 74% and (PI) 55%. Noticeably, after a week of aging, these values changed to (PL) 39.4,

5

(LL) (Casagrande method) 294.5% and (PI) 255.1%. These values are consistent with the high smectite content in this sample.

3.2. TXM results and discussion

The smectite flakes in the TXM micrograph of a completely dispersed sample of 2.5 wt% in DI water suspension (Fig. 2A) clearly display a flocculated microstructure. Flocks seen in this micrograph look like an assembly of smaller particles; their dimensions range up to 1.5 μm and they tend to be interconnected with neighbouring flocks, leaving more or less apparent interflock voids. The thickness of the sample shown in this micrograph is approximately 250 μm. As much as 50 μm can be seen in focus, showing that many of the structural elements, such as particles and voids, can overlap each other. This effect may reduce measured porosity values from the space images seen in the 2D TXM micrographs such as those in Fig. 2. Structural elements like particles, flocks and voids observed in these images appear elongated. The low value of the anisotropy coefficient in the dispersed sample was K_α - 9 %; this value testifies to the low orientation of structural elements towards each other. The low orientation value in the examined sample demonstrates that particles are organised with some level of ordering. Submicron flakes build elongated chains. Fig. 2A shows nearly vertical lineaments where elongated structural elements tend to be arranged in more or less parallel orientation towards similar neighbouring chained elements. However, most flakes are not associated with these chains and form a sort of haze with extremely dispersed constituents—probably loosely attached ultrafine particles that appear in the image as cloudy masses filling most intra-aggregate voids. A few larger voids less affected by this extremely dispersed phase are visible in divisions between larger flock clusters. The porosity value, as measured from the TXM images shown in Fig. 3 (2.5 wt% aqueous suspension), was 28 % and the average void diameter was 480 nm.
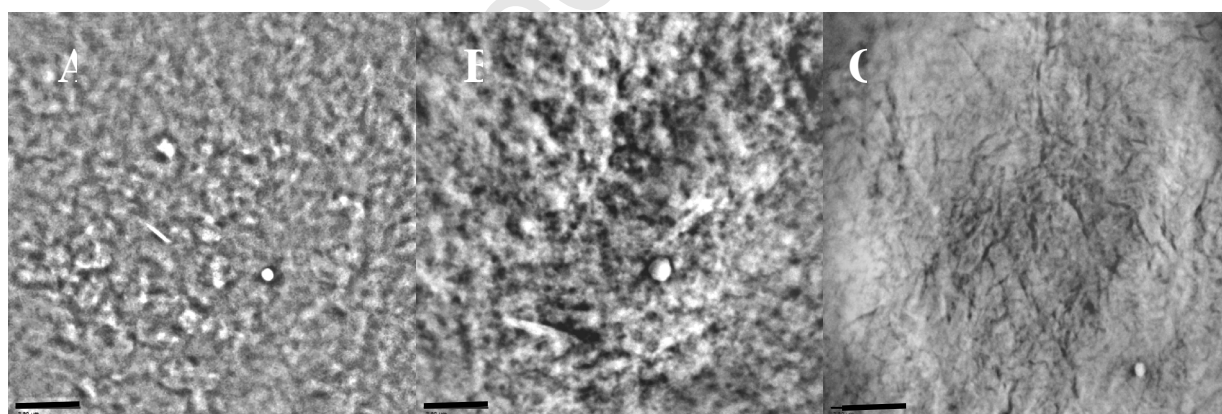

Fig. 2. TXM micrographs of flocked 'Amcol' smectite: (A) 2.5 wt% aqueous suspension; (B) in close to the LL condition; (C) in close to the PL condition (scale bars 2.5 μm). The spherical particle near the middle of the micrographs is a nano-gold particle inserted for picture aligning.

The near LL condition sample was prepared from the powder sample prior to TXM examination. This sample (Fig. 2B) shows densely flocked aggregates. None of the fluffy loose particles seen in the dispersed sample was observed in the LL condition. The microstructure looks cellular, with densely flocked aggregates surrounding clearly visible voids of mostly regular shapes. Some voids, circular in shape, probably contain air microbubbles introduced during sample

6

handling. The structural element median dimension calculated from TXM images and shown in Fig. 3 is 360 nm and the porosity value is 25%. The level of ordering in this sample looks higher than in a suspension. The anisotropy coefficient of this microstructure, calculated as a median value from 100 images, is higher than measured in suspension ($K\alpha$ - 17%), which points to a higher orientation of structural elements than in the suspension sample. This structural anisotropy may be an effect of sample handling when the mineral powder was worked with water to near the LL condition.

A sample prepared near to the PL condition was also prepared from the powder sample prior to TXM examination. This sample, shown in Fig. 2C, displays massive microstructures with densely flocked aggregates and elongated fissure-like voids that cut the sample in different directions. The structural element median dimension calculated from TXM 3D images (Fig. 3) is 220 nm and the porosity value is 11%. In term of structural element orientation, this sample displays a higher anisotropy coefficient of structural elements ($K\alpha = 35\%$) than the sample in DI suspension and in the LL condition. As this sample was worked prior to examination from dry mass, this orientation of structural elements may be the result of intense preparation.
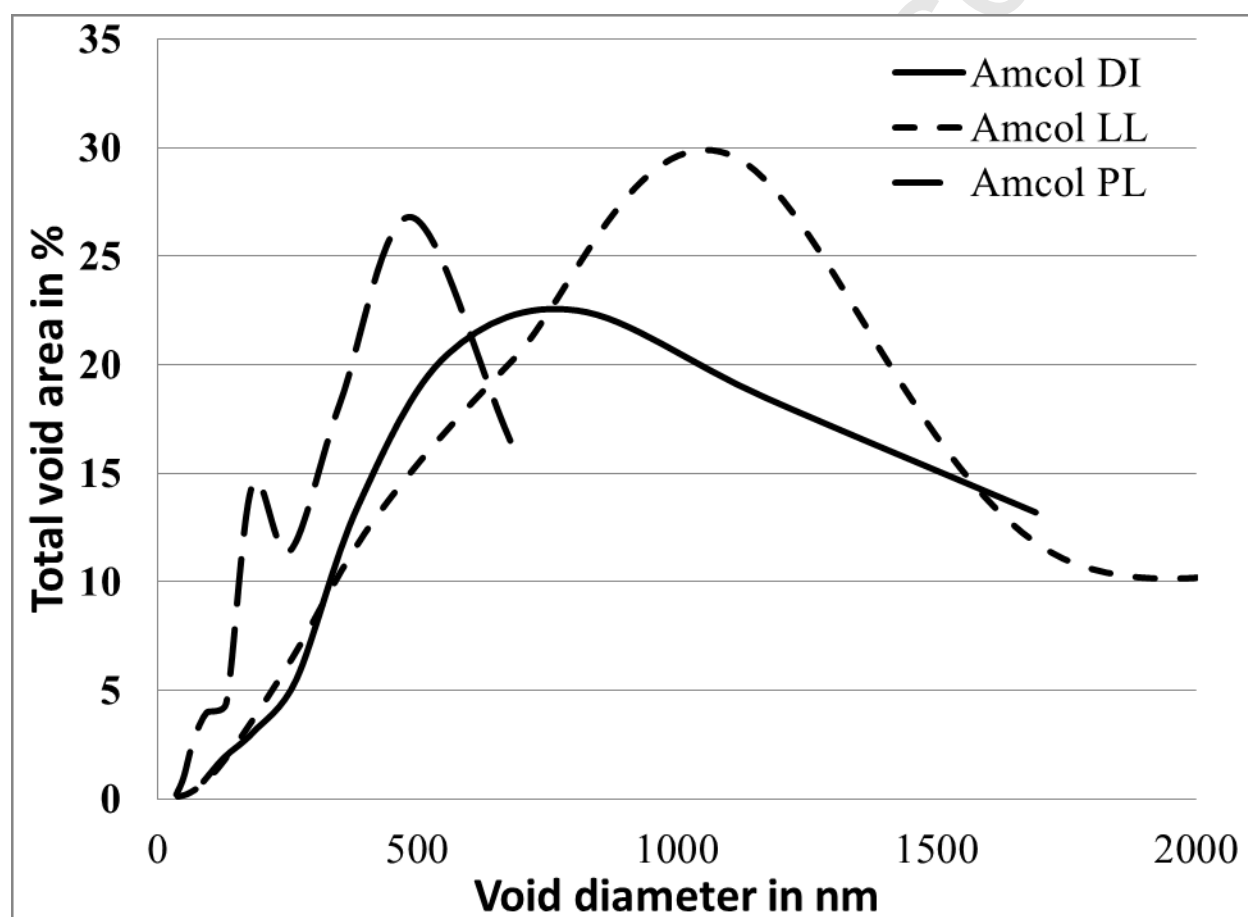
Fig. 3. Total void average diameter versus total void area distribution from TXM images.
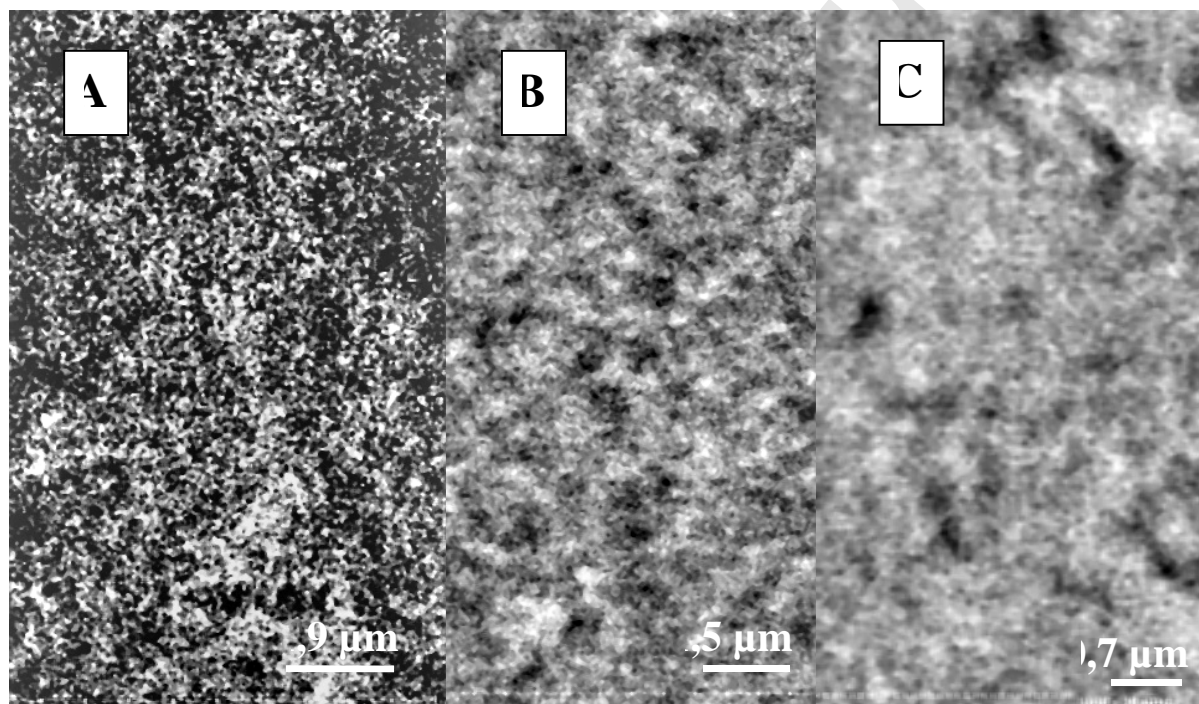
Slightly different results were obtained from analysing 2D sections from computer-reconstructed tomography images. These sections, shown in Fig. 4, were significantly thinner than the original space TXM images; their thickness was approximately 30 nm. However, these sections were not original images; rather, they were produced by computation by integrating all images that were subject to a particular sample tomography.

7

The sectioned tomography reconstruction image in Fig. 4A shows the internal structure of a smectite suspension in DI water that had been well dispersed and seasoned in water for a few weeks. Individual smectite flakes seen in TXM images (DI suspension) form a voluminous space network in which most platelets connect to each other at their edges (EE) and tend to be perpendicular in orientation with a significant angle twist. This peculiar structural arrangement of flakes formed short chains and a spiralling habit because of the twisted position of interconnected flakes. Aggregates observed in the magnified micrograph (Fig. 4A) display long and twisted chains of flakes that form a lengthy and extremely porous spanned framework. In some places, denser flakes in concentrations of up to a few microns can be seen, denser flocks and larger aggregates immobilised within this network were also observed.

The type of microstructure described above has been observed previously and classified as the new model 'net of flakes' [15], closely related to the 'house-of-cards' structure proposed in the 1920s [16, 17]. Such a network remains stable as platelets support each other with electrostatic forces against the much weaker gravitational force and so prevents the suspension from settling.

The void median dimension, as seen in the aqueous suspension shown in Fig. 5, was calculated from the TXM tomography section. It was 140 nm with a porosity value of 43%.

Fig. 4. TXM computer-reconstructed sections ~30 nm thick: (A) The 2.5 wt% aqueous suspension shows the networking of clay flake-like particles into a spanned framework in which twisted smectite flakes connect at their edges (EE) and form an extremely porous microstructure that may be classified as the 'net of flakes' model; (B) This section, prepared close to LL, shows swelled porous interconnected aggregates surrounded by larger water-filled interconnected voids; (C) This section, prepared close to the PL, shows swelled porous interconnected aggregates densely packed, surrounded by narrow water-filled voids. This section exhibits low porosity structure with some intra-aggregate voids that retain water.

8

The section of the sample observed in near LL, shown in Fig. 4B, looks very different to these seen in TXM micrographs. In this micrograph, lumps of dense aggregates connect to the spanned network of cellular type with enclosed voids between clay aggregates. In such a structure, water is most likely retained and cannot be freely drained. The void median dimension, as seen in the aqueous suspension and shown in Fig. 5, was calculated from the TXM tomography section. It was 122 nm with a porosity value of 17%. Lumps of relatively densely flocked aggregates, connected to the spanned network, can be seen in the TXM micrograph. The average diameter of these aggregates was estimated at 500 nm. The enlarged picture in the section image (Fig. 4B) shows that these aggregates were cellular, relatively porous and consisted of randomly oriented platelets and aggregates of approximately 100 nm in dimension.

The section image of the sample observed near to PL, shown in Fig. 4C, displays a massive lump of aggregates with the lowest porosity values and number of pores. The flock median dimension, as seen in the aqueous suspension and shown in Fig. 5, calculated from the TXM tomography section, was 90 nm and had a porosity value of 3.2%. It is difficult to estimate the flock average size because the flocks were all connected into a single massive body. From the high-magnification image (Fig. 4C), it may be seen that this massive body consists of smaller densely flocked aggregates with diameters of 350–400 nm. Such an aggregate exhibits a more dense porous structure than the microstructure observed in the LL sample. Structural elements like particles and pores in observed flocked aggregates remain well below 100 nm of the resolution limits in these computer-generated images.
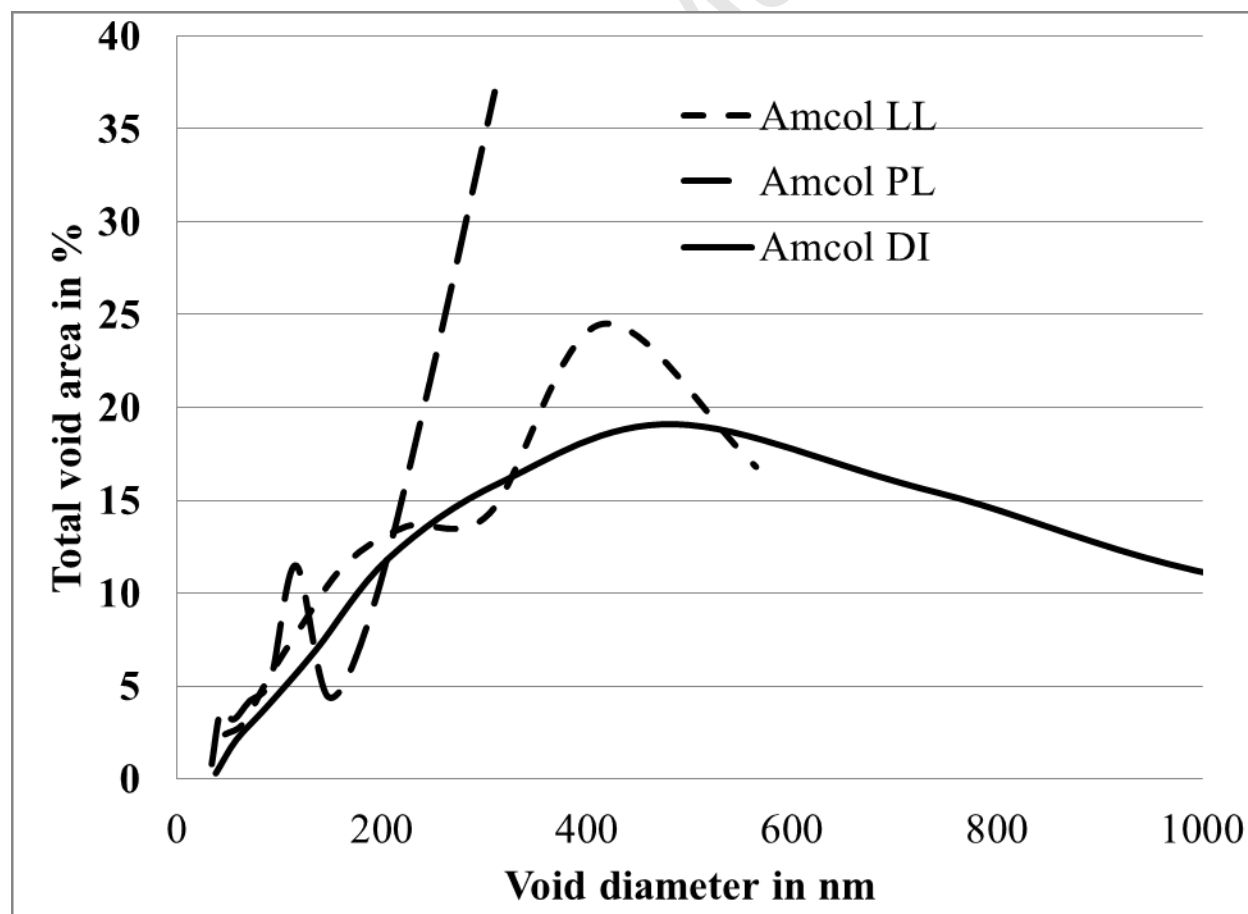

Fig. 5. The total void diameter distribution in the function of void area from a 2D cut section of the TXM reconstructed 3D model.

Fig. 5 shows that the aqueous suspension displays a broad range of voids from 80 to 900 nm, with a positive correlation between the total void area and diameter. The void diameter distribution pattern for LL and PL samples was completely different: the maximum diameter for the LL sample was approximately 400 nm while for the PL sample, it was approximately 300 nm.

A comparison of "stereo-pars" of TXM micrographs examined under a 1-degree rotation angle difference using STIMAN 3D software also delivered interesting data. The results of the comparison are plotted in the structural elements size distribution diagram shown in Fig. 6. These results were plotted against particle size distribution (PSD) according to particles volume conducted on an Amcol bentonite powder sample, which was dispersed in water immediately prior to measurement. On the secondary axis, a volume density particle distribution curve complements the PSD results on the primary axis.

The PSD results from the bentonite powder sample demonstrate a broad particle distribution ranging from 0.5 to more than 100 μm. The median value of Amcol PSD particle sizes was ~8 μm, with the average particle size being 30 μm. Two major maxima can be seen in the volume particle distribution curve, with one maximum at approximately 0.9 μm and the second at approximately 3.5 μm. These groups of particles belong to clay minerals and represent mostly smectite flakes and their primary non-delaminated aggregates as well as an admixture of kaolinite. A small refraction in the higher particle distribution curve may testify to the existence of a third maximum with a particle diameter of approximately 50 μm. These particles may represent smectite primary non-delaminated aggregates as well as non-clay minerals such as quartz. It is noticeable that nanoclay flake-like particles with diameters of 30–500 nm, which were observed in most TEM micrographs, were not represented in the PSD Malvern Mastersizer results. This phenomenon may be explained by the fact that PSD results were plotted by particle volume not by number. These nano-clay particles observed in TEM images may be numerous by quantity but they are negligible if counted by their volume or mass. Another explanation may be that the laser method, designed for recognising spherical shaped particles, cannot detect such small and high aspect ratio plate-like particles.

The structural elements size distribution curves in Fig. 6 cover a very narrow range of diameters between 0.5 and 3 μm. This range covers the majority of the clay minerals equivalent diameters that may be present in the studied sample in the liberated form of singular platelets and small aggregates. For the purpose of the TXM examinations, places were chosen to observe structural elements that fit the frame dimensions (16 x 16 μm). Larger objects were not suitable for examination using this method and were not studied.
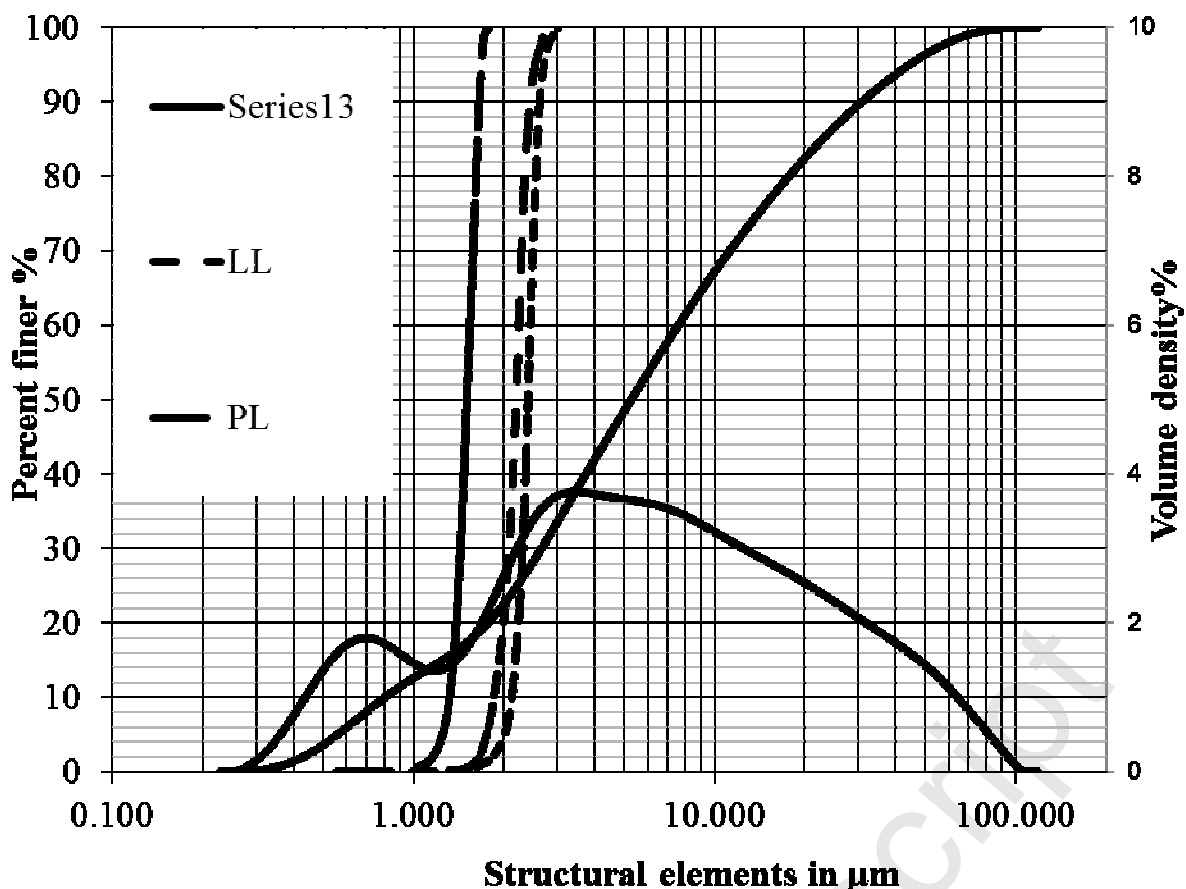
10

Fig. 6. Continuous line Amcol PDS diagram showing particle size distribution (primary axis) and total particle volume density (secondary axis). The dashed lines show the structural elements size distribution calculated from TXM stereo images (primary axis).

The TXM results curves from the DI suspension and LL samples were very close together. The suspension sample median diameter of structural elements was 2350 nm. This was larger than the measured size of structural elements in the near LL condition sample. The median diameter of structural elements for LL was 2120 nm. The close structural similarities between the samples can be explained by the fact that the samples' clay framework was placed in a liquid environment. The larger structural elements noticed in the DI water suspension than in the LL sample may be the result of the larger space available in the low-density water suspension. In such a seasoned suspension, clay aggregates may delaminate and form a mature, almost isotropic structural framework. The nano-clay particles were not noticeable in the TXM structural elements size distribution because they were below the resolution of the equipment and because of their strong association to aggregates.

The smallest median diameter value of structural elements was approximately 1460 nm and was obtained for dense flocks of the clay sample in near PL condition. Volumes occupied by structural elements in PL condition were three times smaller than volumes occupied by structural elements in LL condition. This may be because significant volumes of water (~255–300%) were removed during the sample from LL to PL stage.

The samples for LL and PL imaging were prepared immediately prior to placement in microscope holders. TXM observations were conducted using time lapse from preparation to data collection over several hours. As the Amcol sample was crushed and milled into a powder of primary bentonite rock, most of the grains were non-delaminated rock fragments, as seen in

11

the SEM micrographs in Fig. 1B. Only a small portion of flaky smectite crystals appears to be liberated.
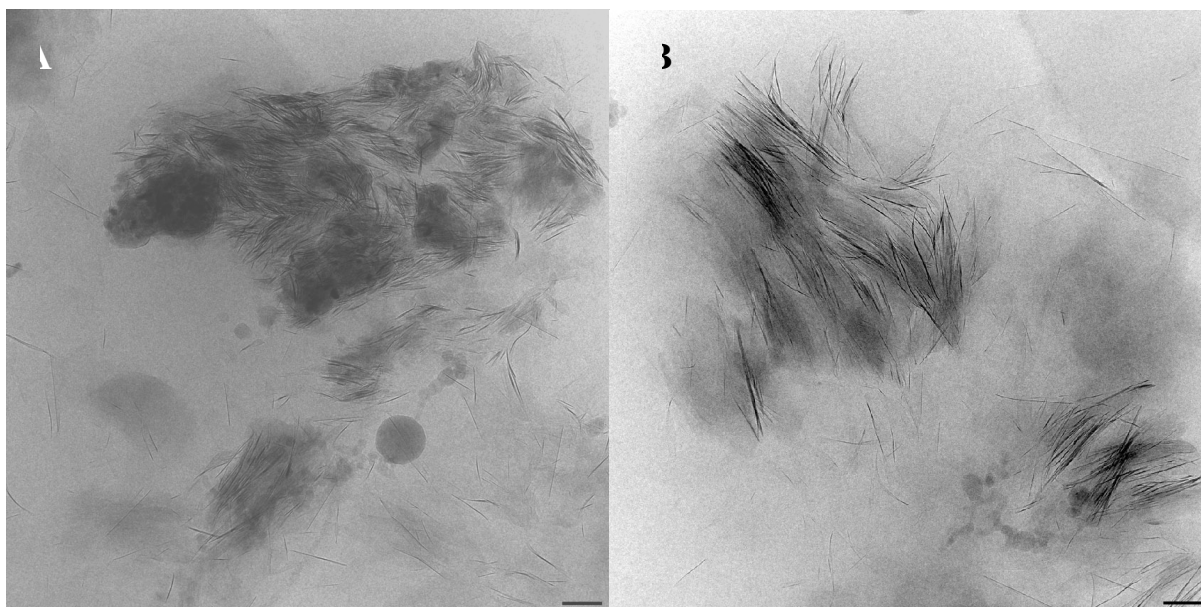
Fig. 7. Cryo-transmission electron microscope (Cryo-TEM) micrographs show Amcol smectite aggregates in vitrified water suspension (scale bars 100 nm).

The contact time between non-delaminated bentonite fragments and water may not have been long enough to disperse the clay flakes from the massive primary grains. This is evident in Fig. 7, in which stacks of smectite crystals can be seen at various stages of delamination and fragmentation. The Amcol bentonite deposits in Miles (Queensland) are of Upper Jurassic age [6]; their primary smectite crystals have been densely packed and preserved within rock stratum for approximately 140 million years. It is not surprising that after such a long detention, the liberation process is not fast. In Fig.7A, aggregates of a few swollen smectite stacks appear loosely connected by the uneven and hairy edges of partially delaminated crystals. Fig. 7B displays 0.5 μm smectite stacks with visible delaminating in process. Highly flexible sheets of high aspect ratio (~200) flakes appear separately or in batches. They are frequently curved and can be seen in various stages of separation from the primary smectite crystal. Many singular flakes, already separated, can be seen in the background of the micrograph.

Micrographs such as those in Fig. 7 illustrate the importance of an understanding of not only mineral composition but also age, genesis and the aging process when studying the physical properties of clay-rich samples. As the rock fragment, to liberate clay particles require a prolonged aging process in water solution, the young soil with secondary deposit may demonstrate their full liberation just after wetting.

Noticeably different values were obtained for the same sample when it was studied directly and after one week of aging. For example, the value of PL without aging was 20%; after aging, it was 39%. Without aging, the LL was 74% and the PI 54%; after aging, the LL was 294% and the PI was almost five times larger, equalling 255%. Cryo-TEM observations suggest that a longer aging process would further liberate clay sheets from primary rock fragments and crystal stacking, effecting a change in physical properties that may further raise Atterberg limits values.

12

Smectite, is the most dispersed member of the clay mineral group, represents a 2:1-type layer silicate forming flaky crystals of extremely aspect ratio [20]. With the expandable structure comprising sheets carrying an excess negative layer charges are linked by weak van der Waals forces. Because of this they may easily expand in water and form nanosuspension. Smectite crystals carrying high electric charge result in the high value of electrokinetic potential (Table 1). This potential reflects the electrical double layer thickness [7, 8] which influence water retention on particles.

Data in Table 1 show that the electrokinetic potential was ionic strength sensitive. The electrokinetic potential measured in DI water has a high value at -61.4 mV. So smectite flakes experience strong electric repulsion forces when approaching each other especially in face to face orientation. However, the small surface area of smectite edges may result in relatively low electrostatic repulsion between particle edges. So, the van der Waals attractive forces may prevail, and edge to edge contacts between smectite thin flakes become favourable in the colloidal system observed in TXM micrographs where most platelets were seen to form chains and be connect in (EE) configuration.

Increase of the pore water ionic strength by adding monovalent salt (0.1 M NaCl) lowers the zeta potential value to -39.6 mV and subsequent the ionic strength increase by adding bivalent salt (0.1 M $CaCl_2$) drops the zeta potential further to -12.6 mV. It is important to understand that water lose by evaporation significantly increases the pore water ionic strength which influences not only inter-particle forces but also water retention within soil. This may consequently alter the Atterberg limits, which will be a focus in our further studies.

4. Conclusion

This study has found that clay particles in aqueous suspension form a spanned framework in which mineral particles, aggregates and water-filled voids establish hierarchic structural elements. The size of these structural elements was found to be largest in water suspensions and to become smaller as a result of water loss in LLs and PLs water content conditions.

The structural element dimension was 2.35 μm (suspension), ~2.12 μm (LL) and ~1.5 μm (PL), with the average diameter of the water-filled inter-floccules and mostly interconnected voids between these structural elements ~480 nm (suspension), 365 nm (LL) and 220 nm (PL).

Voids within structural elements, mostly closed, intra-floccules voids were much smaller; their median diameter was calculated as 140 nm (suspension), 120 nm (LL) and 90 nm (PL).

The clay suspension structure in DI water was almost isometric, with a low anisotropy coefficient of Kα -9 %, but with an increased structure anisotropy in LL (Kα - 17%) and PL (Kα - 35%). The increase of anisotropy in the samples studied was most likely a result of the sample having been worked to achieve the required LL and PL water-content conditions.

Non-delaminated smectite crystals were observed in clay suspension and exhibited different Atterberg limits values depending on their aging period. Sample geological age and genesis were

13

indicated as important factors, alongside mineral composition, in predicting soil's physical behaviour. Because of the high dispersion, high aspect ratio and high electrical charge in smectite crystals, smestite rich soils display expansion and unusual structure building phenomenon when wetted. This plays a crucial role in the unusual behaviour of smectite bearing cohesive soils. Therefore, careful consideration of the sample mineral composition, clay content and genesis must be given, alongside the soluble salt composition and content, in preparing soil samples for geotechnical examination.

Acknowledgements

References

[1]   A.J. Wesselink, Heat conductivity and nature of the lunar surface material, B Astron I Neth 10, (390) (1948) 351–363.

[2]   T.W. Lambe, R.V. Whitman, Soil Mechanics, SI Version, John Wiley & Sons , New York, 1979.

[3]   T.W. Lambe, Soil Testing for Engineers, John Wiley & Sons, New York, 1951.[4] D.P. Coduto, 1999. Geotechnical Engineering: Principals and Practices. Prentice Hall. New Jersey.)

[5]   J-L. Briaud. Geotechnical Engineering. Unsaturated and saturated soils. John Wiley & Sons Inc. Hoboken, New York, Canada, 2013

[6]   N.F. Exon, P.G. Duff, Jurassic Bentonite from the Miles District, Queensland, Department of National Development, Bureau of Mineral Resources Geology and Geophysics, 1968.[7] R.J. Hunter, Zeta Potential in Colloids Science, Academic Press, New York, 1981.

[8]   J. Lyklema, Electrokinetics after Smoluchowski. Colloids and Surfaces A: Physicochem Eng Aspects 222 (2003) 5–14.

[9]   M. Minor, A.J. van der Linde, H.P. Leeuwen, J.J. Lyklema, Dynamic Aspects of Electrophoresis and Electroosmosis: A New Fast Method for Measuring Particle Mobilities. J Colloid Interface Sci. 189 (1997) 370–375.

14

[10]   D. Attwood, Nanotomography comes of age. Nature 442 (2006) 642–643.

[11]   G.C Yin, M.T. Tang, Y.F. Song, F.R. Chen, K.S. Liang, F.W. Duewer, W. Yun, D.H. Ko, H.-P.D. Shieh, Energy-tunable transmission x-ray microscope for differential contrast imaging with near 60 nm resolution tomography. Appl Phys Lett 88 (2006) 241115-1– 241115-3.

[12]   Y.M. Sergeev, G.V. Spivak, A.Y. Sasov, V.I. Osipov, V.N. Sokolov, E.I. Rau, J Microsc Quantitative morphological analysis in a SEM microcomputer system I Quantitative shape analysis of single objects. Morphological analysis of complex SEM images. 135 (1983) 1–12.

[13]   Y.M. Sergeev, G.V. Spivak, V.I. Sasov, V.I. Osipov, V.N. Sokolov, E.I. Rau, J Microsc Quantitative morphological analysis in a SEM microcomputer system II. Morphological analysis of complex SEM images. 135 (1983) 13–24.

[14]   V.N. Sokolov, D.I. Yurkovets, O.V. Ragulina, V.N. Mel'nik, Bull Russ Acad Sci Phys 68 Study of characteristicks of rocks microstructure with aid of SEM micrographs analyse. (2004) 1491–1497.

[15]   V.N. Sokolov, O.V. Razgulina, D.I. Yurkovets, M.S. Chernov, Quantitative Analysis of Pore Space of Moraine Clay Soils by SEM Images. J Surf Investig-X-Ra, 1(4) (2007) 417–422.

[16]   P. Smart, N.K. Tovey, Electron Microscopy of Soils and Sediments: Techniques, Clarendon Press, Oxford, UK, 1982.

[17]   M.S. Żbik, D.J. Williams, Y.-F. Song, Ch.-Ch. Wang, The formation of a structural framework in gelled Wyoming bentonite: Direct observation in aqueous solutions. J. Colloid Interface Sci 435 (2014) 119–127.

[18]   K. Terzaghi, Erdbaummechanik auf Bodenphysikalischer Grundlage, Franz Deuticke Press, Leipzig, Germany, 1925.

[19]   A.J. Casagrande, The structure of clay and its importancein foundation engineering. Boston Soc Civil Eng 19 (1932) 168–208.

[20]   M. Zbik, R.St.C. Smart, Nanomorphology of Kaolinites: Comparative SEM and AFM Studies. Clays Clay Miner. 46 (2) (1998) 153–160.

15

Figure captions.

Fig. 1. (A) The TEM micrograph shows a small aggregate of 'Amcol' smectite flakes ca. 2 μm in diameter and much smaller plate-like particles seen on a background of particles below 100 nm; (B) SEM micrographs show a smectite primary aggregate that displays flexible smectite flakes just below 1 μm in diameter; (C) The XRD diffractogram shows the presence of smectite (S) as the major constituent alongside a small admixture of quartz (Q), anorthite (An), kaolinite (K) and anatase.

Fig. 2. TXM micrographs of flocked 'Amcol' smectite: (A) 2.5 wt% aqueous suspension; (B) in close to the LL condition; (C) in close to the PL condition (scale bars 2.5 μm). The spherical particle near the middle of the micrographs is a nano-gold particle inserted for picture aligning.

Fig. 3. Total void average diameter versus total void area distribution from TXM images.

Fig. 4. TXM computer-reconstructed sections ~30 nm thick: (A) The 2.5 wt% aqueous suspension shows the networking of clay flake-like particles into a spanned framework in which twisted smectite flakes connect at their edges (EE) and form an extremely porous microstructure that may be classified as the 'net of flakes' model; (B) This section, prepared close to LL, shows swelled porous interconnected aggregates surrounded by larger water-filled interconnected voids; (C) This section, prepared close to the PL, shows swelled porous interconnected aggregates densely packed, surrounded by narrow water-filled voids. This section exhibits low porosity structure with some intra-aggregate voids that retain water.

Fig. 5. The total void diameter distribution in the function of void area from a 2D cut section of the TXM reconstructed 3D model.

Fig. 6. Continuous line Amcol PDS diagram showing particle size distribution (primary axis) and total particle volume density (secondary axis). The dashed lines show the structural elements size distribution calculated from TXM stereo images (primary axis).

Fig. 7. Cryo-transmission electron microscope (Cryo-TEM) micrographs show Amcol smectite aggregates in vitrified water suspension (scale bars 100 nm).

CONTENT:

1. Introduction
2. Experimental section
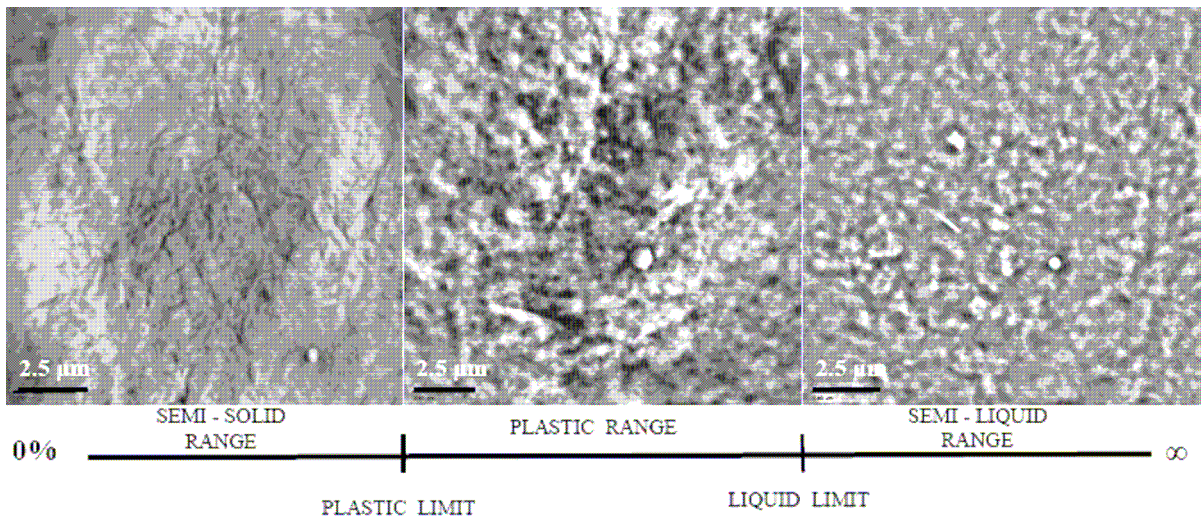**3. Results and discussion**
3.1. General characterisation
3.2. TXM results and discussion
4. Conclusion

16

Acknowledgements

17

18

Highlights

- Microstructural investigation of smectite clay in Atterberg limits was conducted.

- Clay particles form a framework with established hierarchic structural elements.

- The water loss was observed mostly from interconnected, inter-floccules voids.

- Size of intra-flock voids resulting of the water loss on liquid and plastic limits.

- Significant differences in Atterberg limits values were result of sample seasoning.

19